Micromechanical analysis of internal instability during shearing

Shay Haq
BSc (Hons., Pak.), MEng (AIT)
Ph.D. Candidate, School of Civil and Environmental Engineering, Faculty of Engineering and IT, University of Technology Sydney, NSW 2007, Australia.
Email: Shay.Haq@student.uts.edu.au

Buddhima Indraratna
BSc (Hons., Lond.), MSc (Lond.), DIC, PhD (Alberta), FTSE, FIEAust., FASCE, FGS
Distinguished Professor and Director, Transport Research Centre, Faculty of Engineering and IT, University of Technology Sydney, NSW 2007, Australia.
Email: Buddhima.Indraratna@uts.edu.au, Ph: +61 400 213 046

Thanh Trung Nguyen
BEng (Hons), MEng (Saitama), Ph.D. (Wollongong), CPEng, M. ASCE
Research Fellow, Transport Research Centre, School of Civil and Environmental Engineering, Faculty of Engineering and IT, University of Technology Sydney, NSW 2007, Australia.
Email: thanh.nguyen-4@uts.edu.au

Cholachat Rujikiatkamjorn
BEng (Hons), MEng (AIT), Ph.D. (Wollongong), FIEAust., MASCE
Professor, School of Civil and Environmental Engineering, Faculty of Engineering and IT University of Technology Sydney, Sydney NSW 2007, Australia.
Email: Cholachat.Rujikiatkamjorn@uts.edu.au

To be submitted to ASCE International Journal of Geomechanics

No. of Words (without abstract and references): **4800** No of Figures: **13**, No of Tables: **1**

Author for correspondence:

Buddhima Indraratna

Faculty of Engineering and IT

University of Technology Sydney

Sydney, NSW 2007

Australia.

Ph: +61 400 213 046

Email: Buddhima.Indraratna@uts.edu.au

Abstract

Internal instability means that the finer particles pass through the constrictions of the coarser particles at a hydraulic gradient well below that of heave or piping, rendering the soil ineffective for its intended purpose. The soil could make a transition from an internally stable state to an unstable state or vice versa due to shear-induced deformation. The Discrete Element Method (DEM) is adopted in this study to examine and quantify the soil behavior by simulating the quasi-static shear deformation of internally stable and unstable soils at the micro and macro scales. The dense bimodal specimens were sheared under drained conditions following a constant mean stress path in order to investigate the influence of stress heterogeneity. At the macroscale, the peak deviatoric stress was found to be a function of the fines content and the initial void ratios of the specimens. The development of the average number of contacts per particle and the stress transfer to the finer fraction during shearing are discussed. The simulation results innovatively show that a dense specimen could undergo a transition from an internally stable to an unstable soil as it dilates during shear. These numerical results have significant implications on the importance of real-life situations, such as predicting mud pumping in railroad tracks.

Author keywords: Internal Instability, Discrete Element Method, Coordination Number, Stress Reduction Factor, Stress-induced Anisotropy

1 Introduction

Internal instability refers to a phenomenon whereby the fine particles pass through the constrictions of the coarse particles under the action of seepage flow (Indraratna et al. 2015; Kenney and Lau 1985). A much lower hydraulic gradient is needed to erode these fine particles than required to initiate heave or piping failure (Indraratna et al. 2020; Israr and Indraratna 2018; Skempton and Brogan 1994). This can lead to a change in the particle size distribution (PSD) of the soil specimen, thus altering the hydraulic and mechanical properties of the soil. Furthermore, soil foundations often experience deformations such as shear dilatancy under loading, leading to the associated internal instability and erosion resistance due to changes in the fabric, including the pore structure. The soils used in practice may not serve their intended purpose if they are internally unstable. The soil types that are vulnerable to internal instability are usually those that are broadly-graded and gap-graded (Kenney and Lau 1985; Skempton and Brogan 1994; To et al. 2018).

In past experimental studies, significant efforts have been made to study the influence of internal instability on shear behavior (Chang and Zhang 2013; Ke and Takahashi 2015; Xiao and Shwiyhat 2012), whereas the development of internal instability during shearing is not yet fully understood. Several studies (Chang and Zhang 2013; Prasomsri and Takahashi 2020; Trani 2009) have also shown the effects of the initial stress state and the loading condition on the internal erosion of soils, but the detailed micro-mechanism could not be captured with these macroscale laboratory tests. For example, the shear-induced deformation changes filtration characteristics associated with the soil fabric and stress distribution at the microscale demands more insight.

The Discrete Element Method (DEM) has been used to study internal instability (Galindo-Torres et al. 2015; Indraratna et al. 2021; Nguyen and Indraratna 2020; Shire et al. 2014). Hu et al. (2020) studied the influence of suffusion on the undrained shear behavior of an internally unstable soil using DEM coupled with Computational Fluid Dynamics (CFD). Zou et al. (2020) studied the suffusion mechanism using coupled DEM-CFD, and their simulations showed that the erosion ratio of the fine particles was larger when Kenney and Lau's (1985) stability index was lower. Nguyen and Indraratna (2020) studied internal erosion through a novel concept of energy transformation. Indraratna et al. (2021) used the microscale variables from the DEM to mark the boundaries between internally unstable and stable isotropically compressed soils. The coordination number and the stress reduction factor were compared to the constriction-based criterion by Indraratna et al. (2011) and particle-size-based criteria by Kezdi (1979) and Kenney and Lau (1985). The coordination number and stress reduction factor varied consistently with the constriction-based retention ratio in contrast to the particle-size-based retention ratios. Soils were internally stable when the coordination number was greater than 1, and the stress reduction factor was greater than 0.5 (Indraratna et al. 2021). Sufian et al. (2021) studied the influence of stress-induced anisotropy on the gap-graded bimodal specimens using the DEM. However, none of these previous studies could address the transition of the specimens from an internally stable to an unstable state attributed to shear-induced deformation. Furthermore, this study interprets three distinct stages in the development of stress reduction factor for the overfilled fabric cases due to the shear-induced deformation of the dense specimens. In contrast, the previous study (e.g., Sufian et al. 2021) only considered a single stage where the stress reduction factor decreases with the shear-induced dilation of the dense specimens.

In view of the above, this paper aims to characterize the internally stable and unstable soils based on the microscale parameters during shearing, which is the major innovation here. The DEM is used to model the dense bimodal specimens with different gap ratios and non-cohesive fines content. The development of the coordination number, sliding contacts, stress reduction factor, and the directional distribution of the contacts during quasi-static shear deformation were investigated to interpret the data and explain the transition from a stable to an unstable state. The findings of the current study help to predict the potential of internal instability at different stress-state of the soil in the field since the initial stress-state is currently considered to predict the instability potential.

2 Particle Size Distribution Curves

Figure 1 shows a set of 10 gap-graded particle size distribution (PSD) curves of the soil specimens considered for analysis from a previous experimental study (Honjo et al. 1996). These specimens exhibit varying degrees of internal instability (Table 1). Two values of the gap ratios were chosen, i.e., 2 and 3, and the larger gap ratios could not be simulated owing to the excessive computational cost involved, which can be considered a drawback of the current study. The fines content was varied from 10% to 40% in order to simulate all fabric categories from underfilled to overfilled. The Gap-graded soils are ample in numerous geotechnical engineering applications. Examples include alluvial sediment deposits, moraines, glacial tills, waste products from mining processes and rockfill-soil mixtures such as in embankment dams, fouled ballast under railways, and geological hazards, such as debris flows and landslides contributing to the occurrence of gap-graded soils (Langroudi et al. 2013; Zhu et al. 2020). Table 1 shows the gap ratios, fines content, initial void ratio, initial coordination number, initial stress reduction factor, and the number of particles considered in the simulation for each specimen.

3 Simulation Approach

Three-dimensional DEM simulations were performed using an open-source code developed by Kloss et al. (2012). The cubical specimens were simulated with periodic boundaries to have an infinite sample size to avoid any boundary effects (Thornton 2000), and the Hertz-Mindlin contact model was used. The spherical shapes were simulated, and the solid density of particles was considered to be 2650 kg/m^3. Young's modulus and Poisson's ratio of the particles were assumed to be 70 GPa and 0.3, which are relevant to represent common geo-granular materials such as sand (Thornton 2000).

The gravity of the particles was turned off. There were at least 500 coarse particles in each specimen, which was enough to create a representative element volume (REV) (Shire et al. 2014). The specimens were prepared in a dense state which was obtained by setting the value of the coefficient of friction (μ_s) = 0 during isotropic compression. Upon reaching the required stress level, the μ_s value was changed to 0.3, and the specimens were equilibrated with a sufficient number of cycles (Shire et al. 2014). A wide range of values of μ_s has been considered in the literature. Senetakis et al. (2013) determined the range of $0.12 < \mu_s < 0.35$ experimentally for sand particles using a micromechanical interparticle loading apparatus. Huang et al. (2014) recommended using $\mu_s < 0.5$ for element tests in geomechanics and concluded that $\mu_s \geq 0.5$ gives unrealistic results; therefore, this study assumed $\mu_s < 0.5$, i.e., 0.3.

Using a strain-controlled approach, a noninteracting cloud of particles was compressed to a target confining pressure $p' = (\sigma_1' + \sigma_2' + \sigma_3')/3$ = 200 kPa. A strain rate was established to guarantee that the specimens deformed in a quasi-static manner. This was confirmed by maintaining a low value of the inertial number (I_n) < 7.9 x 10^{-5}. The I_n is defined as follows (Da Cruz et al. 2005).

$$I_n = \dot{\varepsilon}\, d_{avg} \sqrt{\frac{\rho}{p'}} \tag{1}$$

where $\dot{\varepsilon}$ is the strain rate, d_{avg} is the average diameter of the coarser fraction of the PSD curve, and p' is the effective mean stress.

In order to bring the particle system into an equilibrium state, the strain rate dropped to zero at p' = 200 kPa. The simulations were executed for additional cycles sufficient to confirm equilibrium. A mean effective stress (p') = 200 kPa was chosen to establish effective contacts between the particles since the gravity of the particles was neglected in the simulations (Shire et al. 2014; Sufian et al. 2021). In addition, 200 kPa is within the range of in situ stress encountered in the field for various infrastructures, including embankment dams and railways. All the PSDs were isotropically compressed to the densest possible state with the same initial values of relative density (>90%) and mean effective stress (200 kPa), similar to the approach used by Shire et al. (2014) and Sufian et al. (2021). The specimens were then sheared under a constant p' stress path (Figure 2) with axial compression and lateral extension. Shearing of the specimens was terminated at an axial strain of 15%. Figure 2b shows the isotropically compressed and deformed DEM specimen at the end of shearing. The average stress tensor of the specimens was calculated using the approach given by Potyondy and Cundall (2004).

4 Results and Discussion

Figure 3 shows the macroscopic stress-strain behavior of the specimens when sheared under drained conditions using a constant mean stress path. Fluctuations in the stress-strain curves are due to the contacts not being engaged during shear (Sufian et al. 2021). The contact engagement depends on the initial fabric of the specimens. For example, the stress-strain curves of Specimens A(40%) and B(40%) show less fluctuations than others in their respective groups, where the fines content is denoted within brackets. A prominent peak deviatoric stress (q_{peak}) is identified in all the specimens at relatively low axial strain values (< 2%), indicating stiff (dense) specimens. It is also clear from Figure 3 that the macroscopic stress-strain response is affected by the gap ratio and the fines content. All specimens show post-peak strain softening; the specimens with higher fines content show a greater reduction in post-peak deviatoric stress, i.e., a greater extent of post-peak strain softening than those with less fines. For example, the post-peak deviatoric stress of Specimen B(30%) at the end of shear is less than that of Specimen B(20%). The stress-strain response of all specimens can also be expressed in terms of brittleness index $(q_{peak} - q_{residual})/q_{peak}$, where $q_{residual}$ is the residual deviatoric stress. The brittleness indices for Specimens B (20%) and B (30%) are 0.42 and 0.61, respectively. A higher brittleness index indicates strain-softening behavior of the specimen with a lower post-peak deviatoric stress. Particle breakage may affect shear behavior in reality; however, this is neglected in the current study due to the added complexity of modeling, which also leads to a high computational effort. It is also noted that different types of particles show different rates of breakage depending on the parent rock type, angularity, and the corresponding stress concentrations. These are obvious limitations of the current study.

Figure 4 shows the development of the volumetric strain (ε_v) with axial strain. The negative value of the vertical axis indicates compression of the dense specimen during the initial shearing phase but is negligible (< 0.005%) (see Fig. 4b & 4d). The DEM results presented in this study are consistent with the observations of Thornton (2000) and Barreto and Sullivan (2012). A positive value of the ε_v indicates the dilation of the specimen. The magnitude of ε_v initially increases until it reaches a critical value and then remains relatively constant. This state is considered to be the critical state, where the shear deformation continues without any change in the specimen volume. The specimens with a higher proportion of fines reach the critical value of ε_v at lower values of axial strain compared to those with a lower proportion of fines. For example, the ε_v of Specimen A(30%) becomes constant at about 6% of axial strain, while for Specimen A(20%), ε_v attains a constant level at an axial strain of about 10%. Similarly, Specimen B(30%) reaches the critical ε_v level at about 5% of axial strain, while Specimen B(20%) shows no apparent convergence of strain to a constant value. For both the gap ratios = 2 and 3, specimens with 30% fines content undergo the least amount of dilation than the other specimens because of the filled fabric, i.e., fine particles completely fill the voids between the coarse particles, restricting the dilation of the specimens.

Figure 5a shows the relationship between the fines content and the initial void ratio (e_o) for each gap ratio. The e_o depends on fines content, gap ratio, and density of the specimen. As the proportion of fines increases, e_o decreases because the fine particles occupy the void spaces between the coarse particles. At a certain proportion of fines, the void spaces are then entirely occupied by the fine particles, as a result of which the void ratio reaches a minimum value. In this situation (Figure 5b), there is no more space available between the coarse particles for accommodating any additional fine particles. If more fines are added, then the separation of the coarse particles will need to occur, and the fine particles then become increasingly more dominant in the mixture. Thus, the coarse particles apparently float in the matrix of fine particles, referred to as an overfilled fabric (Figure 5b). Clearly, the void ratio increases upon reaching the overfilled fabric. The proportion of fines at which the minimum value of e_o is reached depends on the gap ratio; a specimen with a higher gap ratio requires more fines to fill the void spaces. Figure 5c shows the variation of the peak deviatoric stress (q_{peak}) at different values of the fines content. As the proportion of fines increases, e_o continues to decrease, causing the q_{peak} value to increase. At the minimum value of e_o, the maximum value of q_{peak} is reached. The value of q_{peak} decreases after the maximum value since e_o increases with a further increase in the fines content. Hence, the value of q_{peak} inevitably becomes a function of e_o and the fines content.

The numerical results show that at 10-15% fines content, the effect of the gap ratio on q_{peak} is insignificant; however, this effect becomes pronounced when the fines content exceeds 15%. The greater the gap ratio, the larger the q_{peak}; in particular, the largest q_{peak} is about 254 kPa at a gap ratio of 3, but it decreases to about 237 kPa as the gap ratio decreases to 2. As the fines content continues to increase and the soil reaches an overfilled state, the difference between the two curves decreases due to the increasing role of the fines in shear strength. One might expect that the two curves representing different gap ratios could become identical as fines continue to increase (>40%) and play a dominant role in the shear behavior of soils.

Figure 6 shows the constriction size distributions (CSDs) of the coarser fraction for Specimens A and B. It is noteworthy that the CSDs are only plotted for the coarser fraction, as it restricts the migration of fines. From Fig. 6, it can be seen that the constriction sizes at the end of shearing are increased by the dilation of the specimens. As constriction sizes are increased, more fines can be transported, and thus the specimens could become internally unstable.

Figure 7 shows the variation of the coordination number (*Z*) with axial strain. The coordination number (*Z*) is a microscale parameter describing the average number of contacts per particle and is given as follows (Thornton 2000).

$$Z = \frac{2N_c}{N_p} \tag{2}$$

where N_c = the number of contacts; and N_p = the number of particles in the specimen.

During the initial shearing phase, the value of *Z* changes rapidly until it reaches a critical value that remains constant thereafter. The drop in *Z* values can be attributed to the shear deformation, which breaks the contacts between the particles. The initial rapid decrease in the coordination number indicates that the rate of contact breakage exceeds the rate of formation of new contacts. This rate of breakage and formation of new contacts becomes equal at the critical state (Rothenburg and Kruyt 2004). It is evident that the critical value of the coordination number is a function of the PSD and the proportion of fines. For Specimen B(30%), the *Z* value momentarily falls below the critical value. These fluctuations in the *Z* values are due to local instability and increased mobility of the particles. If real boundaries were used, this could lead to strain localization and shear band formation. Strain localization cannot occur in periodic cells when the uniform strain field is applied (Thornton 2000).

Figure 7c shows the percentage drop in Z (ΔZ / Z_o, where Z_o is the initial value of the coordination number) during shear-induced deformation with fines content. The overall behavior can be divided into three categories: (i) the drop in the value of Z is less for specimens with a low fines content, (ii) the value of Z drops significantly for specimens with 20 to 30% fines, but the percentage of drop also depends on the gap ratio, (iii) for overfilled specimens with a greater proportion of fines, the drop in Z is again lower, and this is consistent across different gap ratios. From Fig. 7c, it can be seen that the drop in the value of Z is greater than 80% for specimens that make a transition from an internally stable to an unstable state, i.e., Specimens A(20%), B(20%), and B(30%).

At the isotropic stress state, Fig. 8(a) shows a plot of the percentage (by number) of unconnected cohesionless fine particles within the voids of the coarse particles for different gap ratios and fines content. For a given particle size distribution curve, the gap ratio is the ratio of the minimum particle size in the coarser fraction to the maximum particle size in the finer fraction. It is shown that with 10% (by mass) fines, the percentage of unconnected (suspended) fine particles by number is greater than 90% for both gap ratios (i.e., 2 and 3) considered within the scope of this study. With 20% (by mass) fines, the proportion of unconnected fines by number is around 50% for both gap ratios. In contrast, with higher proportions of fines corresponding to 30% and 40% (by mass), the percentage of fine particles (by number) for both gap ratios is less than 20%. A lower percentage (by number) of unconnected fines at a higher percentage (by mass) of fines indicates that the fines occupy the voids between the coarse particles, thereby establishing contact with one another. From this, it can be concluded that at 10% and 20% of the fines with gap ratios of 2 and 3, a notable number of unconnected fines can still be present in the voids of the coarse particles. Similarly, Fig. 8(b) shows the plot of the percentage (by number) of unconnected fine particles at the end of shearing. It can be seen from Fig. 8(b) that the percentage of unconnected fine particles increased at the end of shearing. This is because the soil dilated and became loose, leaving more free fine particles that are easily eroded.

Figure 9 shows plots of the stress reduction factor (α), axial strain and stress ratio (q/p'). The α is the ratio of the mean stress carried by the fines to the overall mean stress and was calculated using the method described by Shire et al. (2014). The value of α is an indication of how much the fine particles are involved in stress transfer and contribute to the overall stress-strain response, hence it can be taken as an index for assessing the potential for internal instability. A low value of α indicates a high potential for internal instability (Shire et al. 2014). The specimens (Fig. 9) can be divided into two groups with clearly different behavior. The first group is of the specimens with low values of the fines content with underfilled fabric, i.e., Specimens A(10%), A(15%), B(10%), and B(15%). The values of α remain constant with axial strain and stress ratio with minimal changes because the fine particles make no contribution to the deviatoric stress and remain loose within the void spaces of the coarse particle fractions. There is a slight increase in the α value for Specimen B (15%) after the peak stress ratio. This is probably due to the redistribution of the stresses in the finer particles during shearing. The second group is of the specimens with higher fines content, i.e., Specimens A(20%), A(30%), A(40%), B(30%) and B(40%). It can be seen that α changes significantly during shearing. In Specimen B(30%), the α value drops significantly from 1.655 to 0.751; similarly, it decreases from 1.665 to 0.964 in Specimen A(30%). The reduction in α of Specimens A(40%) and B(40%) is not as significant as that of Specimens A(30%) and B(30%). In this regard, for specimens in the second group, the development of α can be divided into three stages. In stage 1, α remains constant for up to a stress ratio = 0.80 with a small value of the axial strain; in stage 2 α decreases slightly as it approaches the peak stress ratio and stage 3 is the post-peak region where the value of α drops significantly. For example, Specimens A(20%), A(30%), A(40%), B(30%), and B(40%), α remains almost unchanged before reaching the peak stress ratio with a small value of axial strain; thereafter, the value of α drops slightly until it reaches the peak stress ratio. After the peak stress ratio, the value of α drops significantly.

For both the gap ratios, the α value increases with the fines content at specific values of the axial strain and stress ratio. As the proportion of the fine particles increases, they begin to participate in the load-carrying process; however, the magnitude of their contribution varies with the gap ratio. For example, with the same proportion of fines, e.g., at 30% of fines, the value of α decreases with an increasing gap ratio. This is because fine particles can easily fit into the voids between the coarse particles as the gap ratio increases. At a higher fines content, i.e., 40%, α increases with the increase in gap ratio because a greater number of fine particles separate the coarse particles and are now available to carry and distribute the stresses (Sufian et al. 2021). For example, the α value at the isotropic stress state of Specimen A(20%) is 1.116 and that of Specimen B(20%) is 0.40. Contrary to this, the α value of Specimen A(40%) is 1.616 and that of Specimen B(40%) is 1.740.

In the previously published study (i.e., Indraratna et al. 2021), a detailed analysis was carried out comparing the initial coordination number (Z_o) and the stress reduction factor (α) and relating them to criteria based on constriction and particle size. A good relationship between the initial coordination number (Z_o), the stress reduction factor (α), and the constriction-based criteria showed that these microscale parameters could be used to assess the potential for internal instability of the soil. A criterion based on the coordination number and the stress reduction factor was proposed to assess the potential for internal instability of granular soils. For instance, specimens with the potential for internal instability had $Z \leq 1$ or $\alpha \leq 0.5$

(Indraratna et al. 2021), which is used in this study. Specimen A(20%) has an initial value of Z = 3.06 and α = 1.116; however, the critical value of Z becomes less than 1, and thus the specimen becomes internally unstable. Similarly, Specimen B(30%) has an initial $Z > 1$ and $\alpha > 0.50$, and thereafter, the value of Z becomes less than unity; hence, it transforms from internally stable to unstable materials with dilation.

In gap-graded soils, the distribution of particle contacts is not uniform for different particle sizes. In this regard, investigating the interparticle contacts between fine-fine and fine-coarse particles during shearing is crucial for understanding the microscale response of soils. Figure 10 shows the evolution of α with fine-fine and fine-coarse coordination number ($Z^{fine\text{-}coarse}$) during shearing, where $Z^{fine\text{-}coarse}$ is defined by (Minh and Cheng 2013):

$$Z^{fine-coarse} = \frac{2(N_c^{fine-fine} + N_c^{fine-coarse})}{N_p^{fines}} \tag{3}$$

where $N_c^{fine-fine}$ is the number of contacts between the fine particles, $N_c^{fine-coarse}$ is the number of contacts between the fine and coarse particles and N_p^{fines} is the total number of fine particles. Although their percentage is lower, the fine particles are much more in number than the coarse particles.

There are three types of fabrics (Shire et al. 2014; Thevanayagam et al. 2002), i.e., (i) Type 1, including Case I and Case IV (Fig. 10), where the coarse particles are mainly in contact with each other. In Case I, the fine particles are loose between the voids of the coarse particles, and the erosion of these fine particles does not significantly disturb the structure of the coarse particles. In Case IV, fine particles are trapped between the coarser particles and are overstressed. (ii) Type 2 is Case II, where the coarse particles are mainly in contact with each other, and the fine particles play a supporting role. Here, both coarse and fine particles influence stress-transfer, but coarse particles govern the transfer of stresses. The loss of fine particles could cause the structure of the coarse particles to collapse, (iii) Type 3, i.e., Case III, where the fine particles are mainly in contact with each other, and the coarse particles are dispersed in the mixture (overfilled by fines). In this case, both the coarse and fine particles transmit equal amounts of stresses. Each case with different intergranular contacts could show a different drained shear response. During the shear-induced dilation of the specimens, a transition in the microstructure between different cases could then occur.

Figure 10 shows the evolution of the fabrics of different specimens with dilation during shearing. For example, Specimen A(20%) is initially with the overfilled fabric in Case III with $Z^{fine-coarse}$ >1 and α >0.5; however, it goes from Case III to Case IV with $Z^{fine-coarse}$ <1 and α > 0.5 at the end of shearing upon the dilation of the specimen. This implies that the fine particles have initially been in contact with each other and have now lost contacts. Similarly, Specimen B(20%) shows Case II with $Z^{fine-coarse}$ >1 and α < 0.5 at the isotropic stress state and transitions to Case I with $Z^{fine-coarse}$ < 1 and α < 0.5 at the end of shearing, implying that fines are now loosely seated between the coarse particles and could be eroded without affecting the coarse particles. These findings are of practical relevance as the specimens could be internally stable with overfilled fabric at the isotropic stress state but could transform from internally stable to unstable soils with underfilled fabric due to shear-induced deformation.

Figure 11 shows the evolution of the coarse-coarse coordination number ($Z^{coarse\text{-}coarse}$) with the deviatoric stress. The value of $Z^{coarse-coarse}$ is defined by (Minh and Cheng 2013):

$$Z^{coarse-coarse} = \frac{2N_c^{coarse-coarse}}{N_p^{coarse}} \tag{4}$$

where $N_c^{coarse-coarse}$ is the number of contacts between coarse particles, and N_p^{coarse} is the number of coarse particles.

The $Z^{coarse\text{-}coarse}$ decreases rapidly until the peak value of deviatoric stress is reached and increases slightly thereafter. At the same time, the stress reduction factor (α) remains constant up to the peak value of the stress ratio (Figure 9). Therefore, during the initial phase of shearing up to the peak of deviatoric stress, the coarse contacts separate due to dilation, while the stresses they carry do not change (constant α), so the reduced coarser contacts become overstressed. After the peak of the deviatoric stress, the loss of contacts stops for the coarse particles while the α drops. As a result, the coarser particles are subjected to greater stress as the α decreases. Because of these higher stresses that the coarse particles carry, they re-establish some contacts after the peak when the $Z^{coarse\text{-}coarse}$ value increases slightly in some specimens (e.g., A(20%), A(30%), A(40%), and B(30%)). This behavior of $Z^{coarse\text{-}coarse}$ is consistent across different specimens, although the initial value of $Z^{coarse\text{-}coarse}$ varies with different fines content.

Figure 12 shows the development of sliding contacts with axial strain. The sliding contacts are defined based on the following equation:

$$S_i = \frac{f^T}{\mu_s f^N} \tag{5}$$

where S_i is the sliding index, f^T is the tangential contact force, and f^N is the normal contact force. Sliding contacts occur when the tangential contact force has fully mobilized the friction, i.e., S_i = 1.

The percentage of the sliding contacts first increases, reflecting the initial shearing stage where the deviatoric stress increases rapidly (see Fig. 3). After reaching a peak value, it decreases and thereafter remains constant, which is when the critical state takes place with constant volumetric strain. It is noteworthy that there is an increase in the percentage of sliding contacts after the peak (axial strain > 3%) in Specimen B(30%). This can be attributed to local instability and increased particle mobility, consistent with the evolution of the coordination number with axial strain for this specimen, as discussed earlier (see Fig. 7).

Figure 13 shows the directional distribution of the contacts (rose histograms) of selected Specimens (A(10%), B(10%), and B(15%) at the isotropic stress state and the end of shearing. These results only apply to the x-z plane since the distribution of the contacts in the y-z plane is similar. From Fig. 13, it can be seen that at the isotropic state of stress, the distribution of the contacts is the same in all directions. However, anisotropy is evolving in the contact networks at the end of shearing, and the contact distribution is not equal in all directions. Therefore, shear deformation of the soil leads to structural anisotropy due to contact separation. The number of contacts in the direction of the major principal stress is greater than that of the minor principal stress. Hence, the major contact losses during shear deformation are in the lateral strain direction perpendicular to the direction of the major principal stress.

4 Practical Applications

The following are some of the practical applications of this study:

- Microscale investigations enabled a better understanding of the mechanism of internal instability of soil, which can be helpful in the design and construction of substructures in railways.
- To demarcate internally unstable and stable soils, the microscale criterion based on the coordination number and the stress reduction factor can be used to estimate the probability of internal instability in the field at different stress state.
- Internal instability is a problem in railways that results in significant maintenance costs. The findings of this study can be used to avoid the huge maintenance cost associated with internally unstable capping layer in railways.

5 Conclusions

This DEM study performed the drained tests following a constant mean stress path to investigate the influence of shear-induced deformation on the micromechanics of internally stable and unstable soils. Based on the findings of this study, the following conclusions could be drawn:

- The results of the numerical analysis showed that the coordination number initially dropped rapidly because the disintegration rate of the contacts was higher than the formation rate of new contacts. It remained unchanged thereafter, as the rate of disintegration and formation of the contacts was the same. This leads to the conclusion that the development of the coordination number was strongly influenced by the shear-induced deformation and the associated internal instability.
- Internally stable specimens, e.g., Specimen A(20%) with initial values of coordination number (Z) = 3.06 and the stress reduction factor (α) = 1.116, transitioned into internally unstable soil with $Z < 1$ and $\alpha > 0.5$ at the end of shearing. Similarly, Specimen B(30%) with initial $Z > 1$ and $\alpha > 0.50$ became internally unstable with $Z < 1$ and $\alpha > 0.50$. The percentage drop in the Z-values of the specimens transitioning from internally stable to unstable soils was greater than 80%. Based on these results, it was evident that the drop in microscale parameters, such as the Z and α values, would be linked to the volumetric response of the specimens at the macroscale.
- It was found that the initial overfilled fabric of Specimen A(20%) with fine-fine and fine-coarse coordination number ($Z^{fine-coarse}$) > 1 and $\alpha > 0.5$ was converted into an underfilled fabric with $Z^{fine-coarse} < 1$ and $\alpha > 0.5$. Similarly, Specimen B(20%), with $Z^{fine-coarse} > 1$ and $\alpha < 0.5$ at the isotropic stress state changed to underfilled fabric $Z^{fine-coarse} < 1$ and $\alpha < 0.5$ at the end of shearing. This leads to the conclusion that the fabric of the soil may change significantly due to shear-induced deformations, thus altering the erosion resistance of the soil.

- The stress reduction factor (α) of specimens with underfilled fabric, i.e., A(10%), A(15%), B (10%), B(15%), and B(20%), remained almost unchanged with the axial strain and the stress ratio. For specimens with a higher fines content, α dropped significantly during shearing. For instance, in Specimen B(30%), α dropped significantly from 1.655 to 0.751. Three distinct stages were interpreted in the development of α, namely: Stage 1, where α was constant when the stress ratio (q/p') $\leq$ 0.80 at a small value of axial strain; Stage 2 represented the slight decrease in α as it approached the peak q/p' and Stage 3 where α dropped significantly in the post-peak region caused by shear-induced dilation. This implies that the stress distribution is a function of the soil fabric, the stress ratio (q/p'), and the axial strain.
- In summary, the shear-induced deformation of the soil affects the coordination number and stress reduction factor. This indicates that the internal instability of the soil is a factor of the stress state of the soil, and the internally stable samples could turn into internally unstable soil due to shear-induced deformation.

Data availability statement

The data will be made available by the authors upon reasonable request.

Acknowledgment

The Authors gratefully appreciate the assistance of Prof Catherine O'Sullivan (Imperial College, London) in reading the manuscript and making constructive comments for its improvement, including the plots in Figure 8. Financial support from the Transport Research Centre, University of Technology Sydney (UTS), Sydney NSW, Australia, is greatly appreciated.

Declaration of competing interest

The authors declare that they are unaware of any competing financial interests or personal relationships that may have influenced the work described in this paper.

Notations

The following symbols are used in this paper:

d_{avg} = average diameter of the coarser fraction of PSD;

G = shear modulus;

I_n = inertial number;

N_p = number of particles;

N_c = number of contacts;

$N_c^{fine-fine}$ = number of contacts between fine particles;

$N_c^{fine-coarse}$ = number of contacts between fine and coarse particles;

N_p^{fines} = number of fine particles;

N_p^{coarse} = number of coarse particles;

$N_c^{coarse-coarse}$ = number of contacts between coarse particles;

p' = effective mean stress of the specimen;

q = deviatoric stress;

R_d = relative density;

r_{min} = minimum particle radius;

Z = coordination number;

$Z^{fine-coarse}$ = fine-coarse coordination number;

$Z^{coarse-coarse}$ = coarse-coarse coordination number;

$\dot{\varepsilon}$ = strain rate;

ε_a = axial strain;

ε_v = volumetric strain;

α = stress reduction factor;

ρ = solid particle density;

ν = Poisson's ratio;

μ_s = coefficient of sliding friction;

σ_1' = major principal stress;

σ_2' = intermediate principal stress;

σ_3' = minor principal stress;

References

Chang, D. S., and Zhang, L. M. (2013). “Critical Hydraulic Gradients of Internal Erosion under Complex Stress States.” *Journal of Geotechnical and Geoenvironmental Engineering*, 139(9), 1454–1467.

Da Cruz, F., Emam, S., Prochnow, M., Roux, J. N., and Chevoir, F. (2005). “Rheophysics of dense granular materials: Discrete simulation of plane shear flows.” *Physical Review E - Statistical, Nonlinear, and Soft Matter Physics*, 72(2), 1–17.

Galindo-Torres, S. A., Scheuermann, A., Mühlhaus, H. B., and Williams, D. J. (2015). “A micro-mechanical approach for the study of contact erosion.” *Acta Geotechnica*, 10(3), 357–368.

Honjo, Y., Haque, M. A., and Tsai, K. A. (1996). “Self-filtration behaviour of broadly and gap-graded cohesionless soils.” *Geofilters’ 96, BiTech Publishers, Montreal, Canada*, 227–236.

Hu, Z., Yang, Z. X., and Zhang, Y. D. (2020). “CFD-DEM modeling of suffusion effect on undrained behavior of internally unstable soils.” *Computers and Geotechnics*, 126(June).

Huang, X., Hanley, K. J., O’Sullivan, C., and Kwok, C. Y. (2014). “Exploring the influence of interparticle friction on critical state behavior using DEM.” *International Journal for Numerical and Analytical Methods in Geomechanics*, (38), 1276–1297.

Indraratna, B., Haq, S., Rujikiatkamjorn, C., and Israr, J. (2021). “Microscale boundaries of internally stable and unstable soils.” *Acta Geotechnica*.

Indraratna, B., Israr, J., and Rujikiatkamjorn, C. (2015). “Geometrical Method for Evaluating the Internal Instability of Granular Filters Based on Constriction Size Distribution.” *Journal of Geotechnical and Geoenvironmental Engineering*, 141(10), 04015045.

Indraratna, B., Nguyen, V. T., and Rujikiatkamjorn, C. (2011). “Assessing the Potential of Internal Erosion and Suffusion of Granular Soils.” *Journal of Geotechnical and*

Geoenvironmental Engineering, 137(5), 550–554.

Indraratna, B., Singh, M., Nguyen, T. T., Leroueil, S., Abeywickrama, A., Kelly, R., and Neville, T. (2020). "Laboratory study on subgrade fluidization under undrained cyclic triaxial loading." *Canadian Geotechnical Journal*, 57(11), 1767–1779.

Israr, J., and Indraratna, B. (2018). "Mechanical response and pore pressure generation in granular filters subjected to uniaxial cyclic loading." *Canadian Geotechnical Journal*, 55(12), 1756–1768.

Ke, L., and Takahashi, A. (2015). "Drained Monotonic Responses of Suffusional Cohesionless Soils." *Journal of Geotechnical and Geoenvironmental Engineering*, 141(8), 04015033.

Kenney, T. C., and Lau, D. (1985). "Internal stability of granular filters." *Canadian Geotechnical Journal*, 22(2), 215–225.

Kezdi, A. (1979). *Soil Physics - selected topics*. Elsevier Scientific, Amsterdam, the Netherlands.

Kloss, C., Goniva, C., Hager, A., Amberger, S., and Pirker, S. (2012). "Models, algorithms and validation for opensource DEM and CFD-DEM." *Progress in Computational Fluid Dynamics, An International Journal*, 12(2/3), 140.

Langroudi, F. M., Soroush, A., Tabatabaie Shourijeh, P., and Shafipour, R. (2013). "Stress transmission in internally unstable gap-graded soils using discrete element modeling." *Powder Technology*, 247, 161–171.

Minh, N. H., and Cheng, Y. P. (2013). "A DEM investigation of the effect of particle-size distribution on one-dimensional compression." *Geotechnique*, 63(1), 44–53.

Nguyen, T. T., and Indraratna, B. (2020). "The energy transformation of internal erosion based on fluid-particle coupling." *Computers and Geotechnics*, Elsevier, 121(February), 103475.

Potyondy, D. O., and Cundall, P. A. (2004). "A bonded-particle model for rock." *International*

Journal of Rock Mechanics and Mining Sciences, 41(8 SPEC.ISS.), 1329–1364.

Prasomsri, J., and Takahashi, A. (2020). “The role of fines on internal instability and its impact on undrained mechanical response of gap-graded soils.” *Soils and Foundations*, Japanese Geotechnical Society, 60(6), 1468–1488.

Rothenburg, L., and Kruyt, N. P. (2004). “Critical state and evolution of coordination number in simulated granular materials.” *International Journal of Solids and Structures*, 41(21), 5763–5774.

Senetakis, K., Coop, M. R., and Todisco, M. C. (2013). “Tangential load-deflection behaviour at the contacts of soil particles.” *Geotechnique Letters*, 3(APRIL/JUN), 59–66.

Shire, T., O’Sullivan, C., Hanley, K. J., and Fannin, R. J. (2014). “Fabric and effective stress distribution in internally unstable soils.” *Journal of Geotechnical and Geoenvironmental Engineering*, 140(12), 1–11.

Skempton, A. W., and Brogan, J. M. (1994). “Experiments on piping in sandy gravels.” *Géotechnique*, 44(3), 449–460.

Sufian, A., Artigaut, M., Shire, T., and O’Sullivan, C. (2021). “Influence of Fabric on Stress Distribution in Gap-Graded Soil.” *Journal of Geotechnical and Geoenvironmental Engineering*, 147(5), 04021016.

Thevanayagam, S., Shenthan, T., Mohan, S., and Liang, J. (2002). “Undrained Fragility of Clean Sands, Silty Sands, and Sandy Silts.” *Journal of Geotechnical and Geoenvironmental Engineering*, 128(10), 849–859.

Thornton, C. (2000). “Numerical simulations of deviatoric shear deformation of granular media.” *Geotechnique*, 50(1), 43–53.

To, P., Scheuermann, A., and Williams, D. J. (2018). “Quick assessment on susceptibility to suffusion of continuously graded soils by curvature of particle size distribution.” *Acta Geotechnica*, 13(5), 1241–1248.

Trani, L. D. O. (2009). “Application of constriction size based filtration criteria for railway subballast under cyclic conditions.” PhD Thesis: University of Wollongong, Wollongong, Australia.

Xiao, M., and Shwiyhat, N. (2012). “Experimental investigation of the effects of suffusion on physical and geomechanic characteristics of sandy soils.” *Geotechnical Testing Journal*, 35(6), 1–11.

Zhu, Y., Nie, Z., Gong, J., Zou, J., Zhao, L., and Li, L. (2020). “An analysis of the effects of the size ratio and fines content on the shear behaviors of binary mixtures using DEM.” *Computers and Geotechnics*, Elsevier, 118(October 2019).

Zou, Y., Chen, C., and Zhang, L. (2020). “Simulating Progression of Internal Erosion in Gap-Graded Sandy Gravels Using Coupled CFD-DEM.” *International Journal of Geomechanics*, 20(1), 04019135.

List of Tables

Table 1. Properties of the particle size distribution curves used in the analysis

S. No.	Specimen ID	Gap Ratio	Fines Content (%)	Initial Void Ratio (e_o)	Number of Particles	Initial Coordination Number (Z_o)	Initial Stress Reduction Factor (α_o)	Internal Stability at the Isotropic Stress State (Indraratna et al. 2021)
1			10	0.3713	5000	0.719	0.459	Unstable
2			15	0.3131	10000	0.858	0.337	Unstable
3	A	2	20	0.2854	12000	3.058	1.116	Stable
4			30	0.3004	20000	4.814	1.665	Stable
5			40	0.3203	30000	5.202	1.616	Stable
6			10	0.3619	15000	0.206	0.044	Unstable
7			15	0.2911	25000	0.146	0.062	Unstable
8	B	3	20	0.2277	35000	2.156	0.400	Unstable
9			30	0.2470	55000	5.141	1.655	Stable
10			40	0.2851	85000	5.419	1.739	Stable

List of Figures

Fig. 1 Particle size distributions (PSDs) of soils analyzed with the discrete element method, (a) PSDs of Specimen A with a gap ratio = 2 with different fines content, (b) PSDs of Specimen B with a gap ratio = 3 with different fines content

Fig. 2 (a) Constant mean stress path followed in the simulations; (b) isotropically compressed and sheared Specimen B(30%)

Fig. 3 Stress-strain curves under drained shearing with a constant mean stress path, (a) for Specimen A, (b) for Specimen B

Fig. 4 Evolution of the volumetric strain (ε_v) with axial strain, (a), (b) for Specimen A, (c), (d) for Specimen B

Fig. 5 (a) Relationship between the fines content and the initial void ratio, (b) schematic sketch of different fabric cases, (c) relationship between the fines content and the peak deviatoric stress

Fig. 6 Constriction size distribution (CSD) of the coarser fraction at the isotropic stress state and end of shearing, (a) Specimen A, (b) Specimen B

Fig. 7 (a), (b) Development of the coordination number (Z) with axial strain for Specimens A and B, (c) percentage of drop in Z values with fines content

Fig. 8 The percentage (by number) of unconnected fine particles with different gap ratios and fines content (a) at the isotropic stress state, (b) at the end of shearing.

Fig. 9 (a), (b) Relationship between stress reduction factor (α) and stress ratio (q/p') for Specimens A and B, (c), (d) relationship between stress reduction factor (α) and axial strain (ε_a) for Specimens A and B.

Fig. 10 Evolution of the stress reduction factor (α) with fine-coarse coordination number ($Z^{fine\text{-}coarse}$) (a) for Specimen A, (b) for Specimen B

Fig. 11 Variation of the coarse-coarse coordination number ($Z_{coarse\text{-}coarse}$) with deviatoric stress, (a) Specimen A, (b) Specimen B

Fig. 12 Development of the proportion of sliding contacts with axial strain, (a) Specimen A, (b) Specimen B

Fig. 13 Rose histograms of the contacts for selected Specimens (a), (b) A(10%), (c), (d) B(10%), and (e),(f) B(15%)

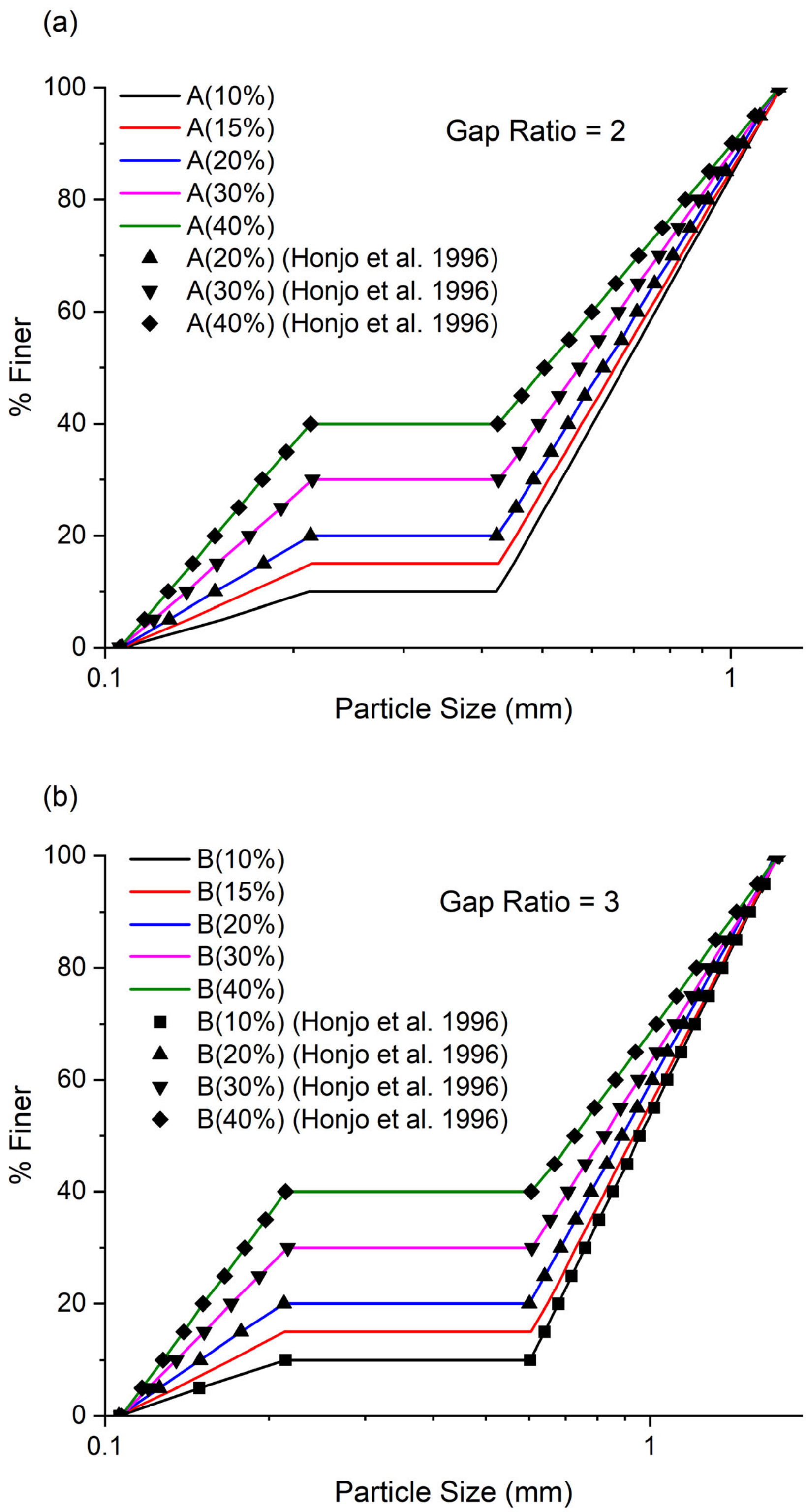

Fig. 1 Particle size distribution of soils analyzed with the discrete element method

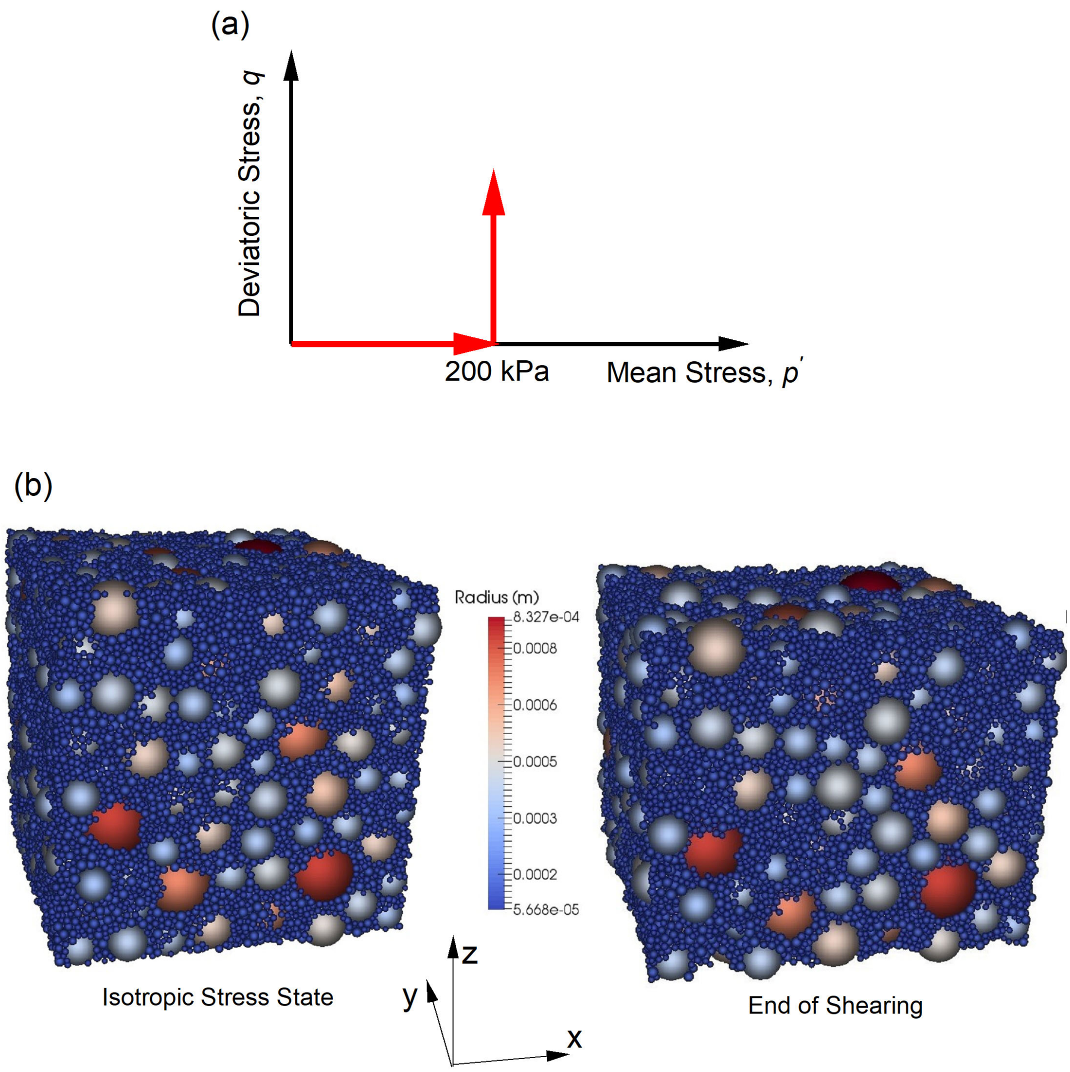

Fig. 2 (a) Constant mean stress path followed in the simulations; (b) isotropically compressed and sheared Specimen B(30%)

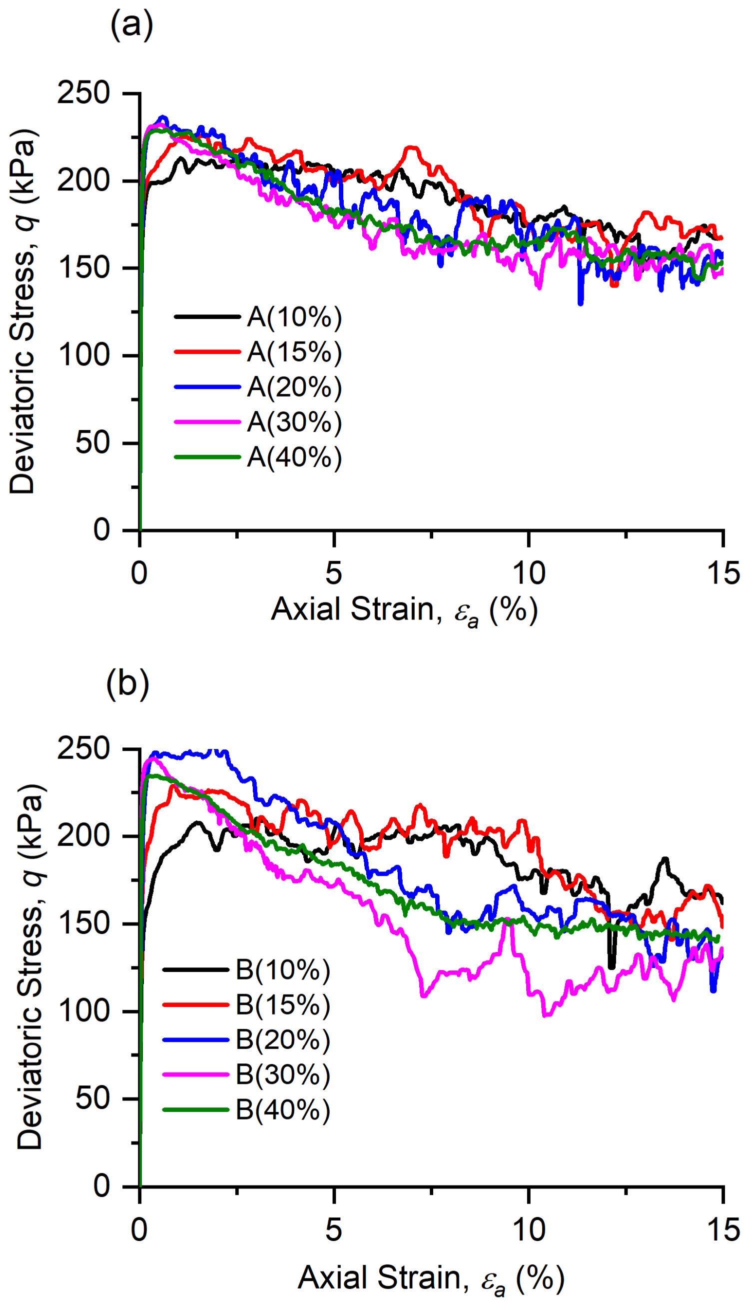

Fig. 3 Stress-strain curves of all specimens under drained shearing with a constant mean stress path

620

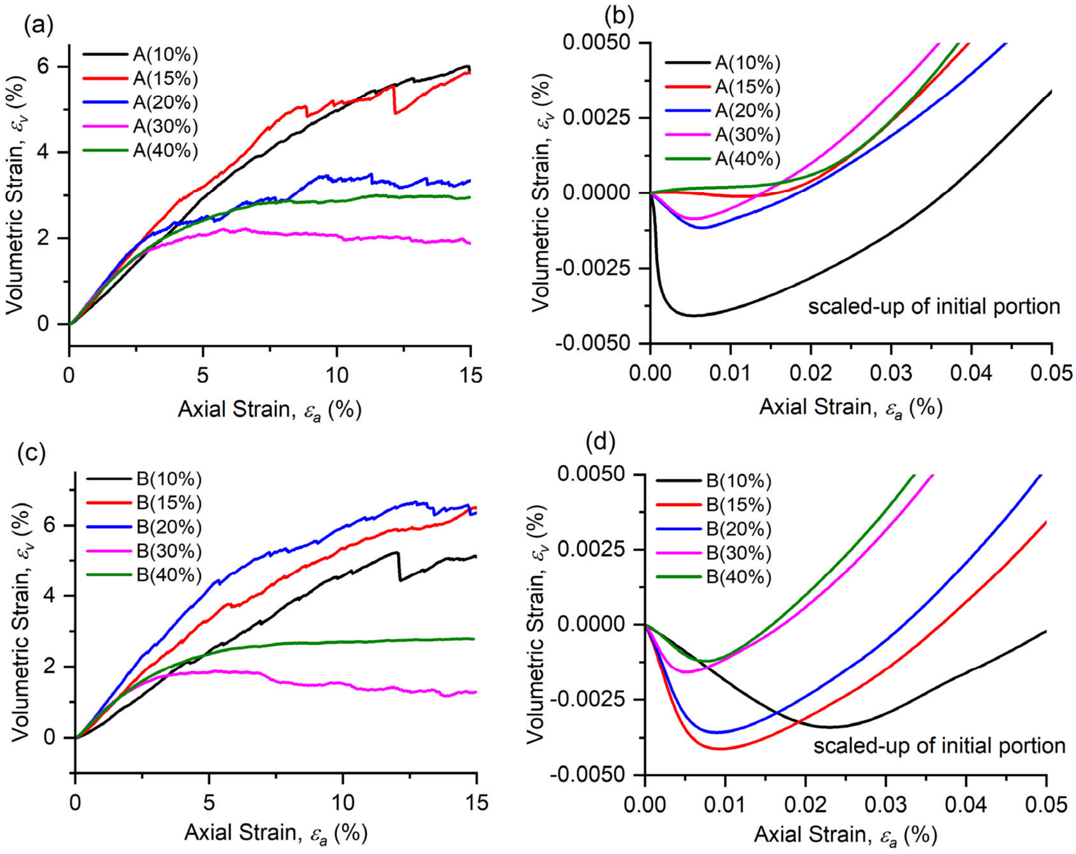

621 **Fig. 4** Evolution of the volumetric strain (ε_v) with axial strain

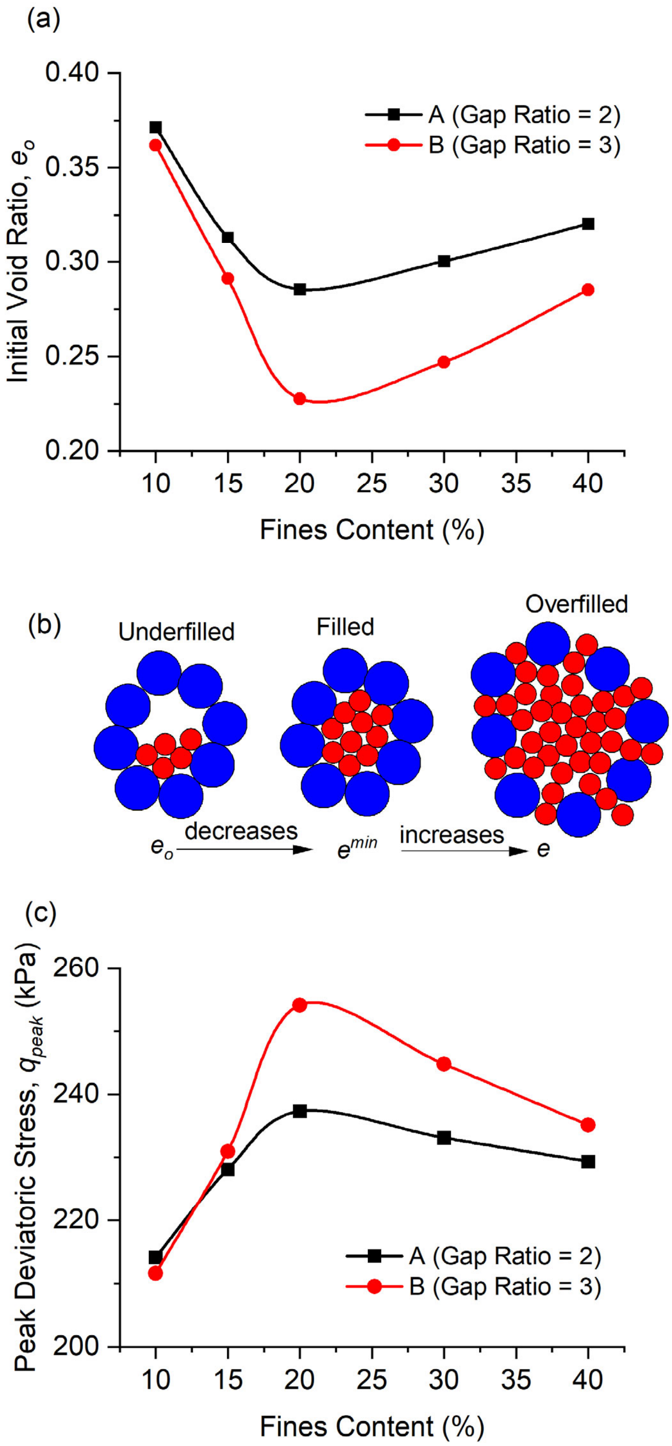

Fig. 5 (a) Relationship between the fines content and the initial void ratio, (b) schematic sketch of different fabric cases, (c) relationship between the fines content and the peak deviatoric stress

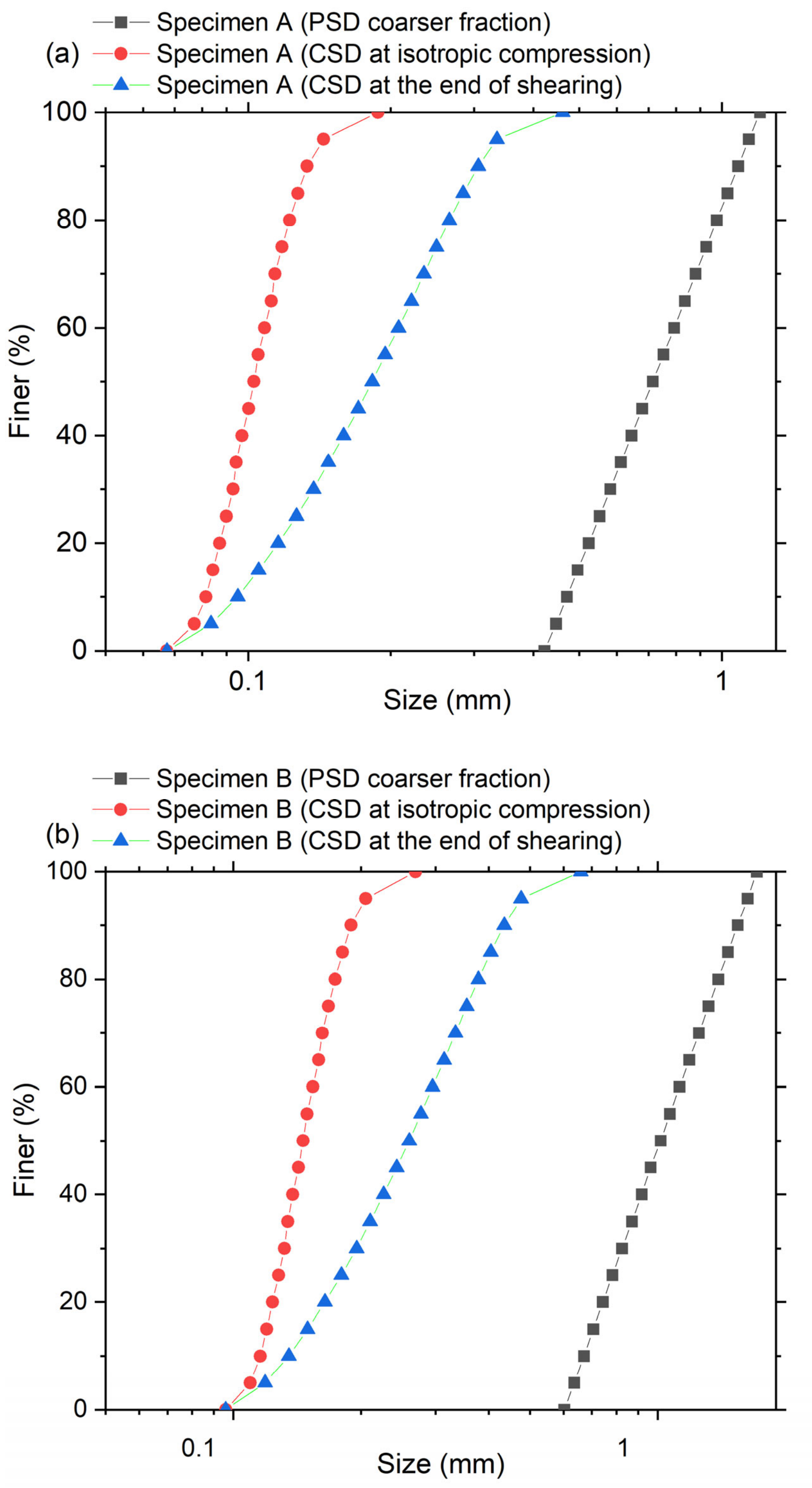

Fig. 6 Constriction size distribution (CSD) of the coarser fraction at the isotropic stress state and end of shearing, (a) Specimen A (b) Specimen B

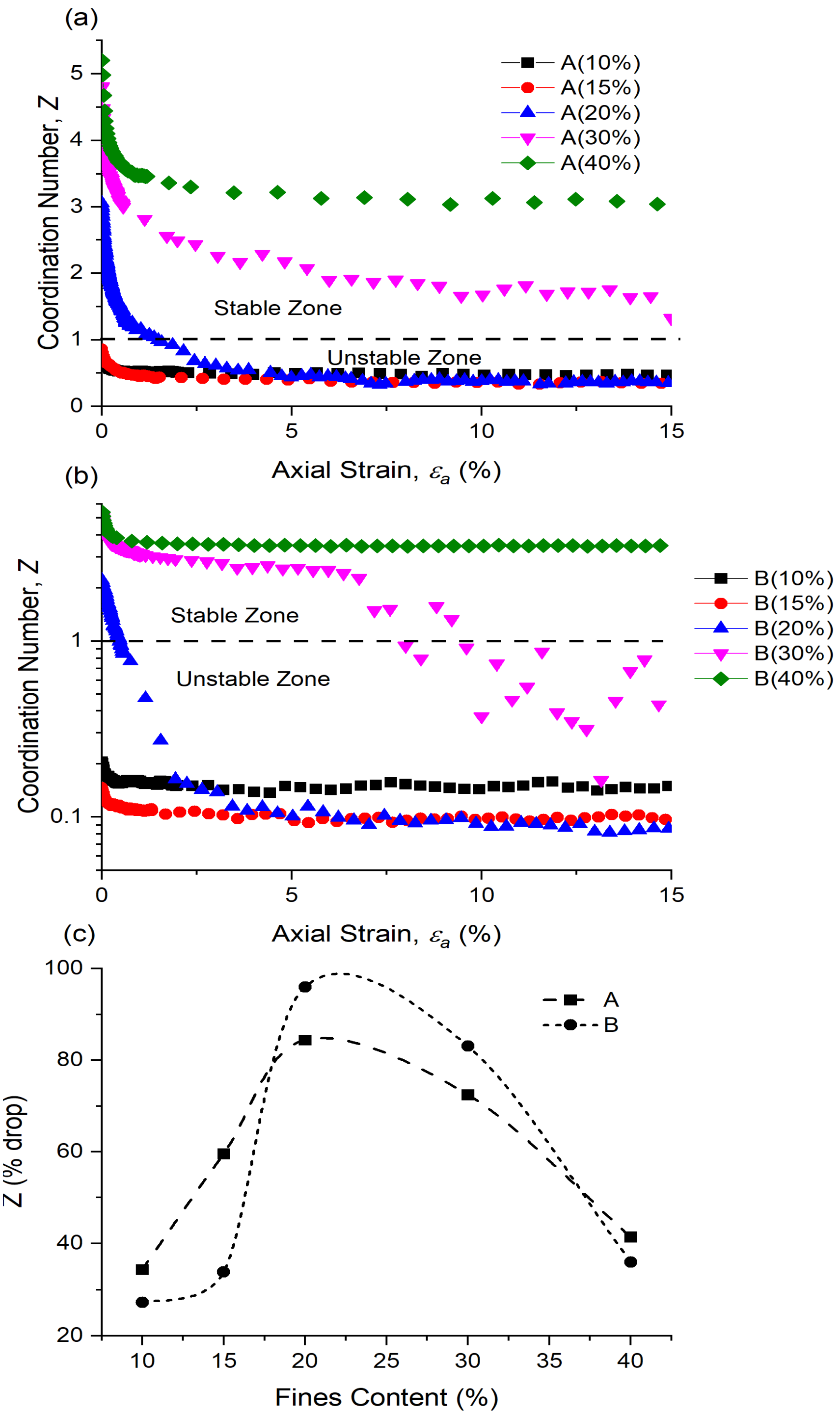

Fig. 7 (a), (b) Development of the coordination number (Z) with axial strain for specimens A and B, and (c) percentage of drop in Z values with fines content

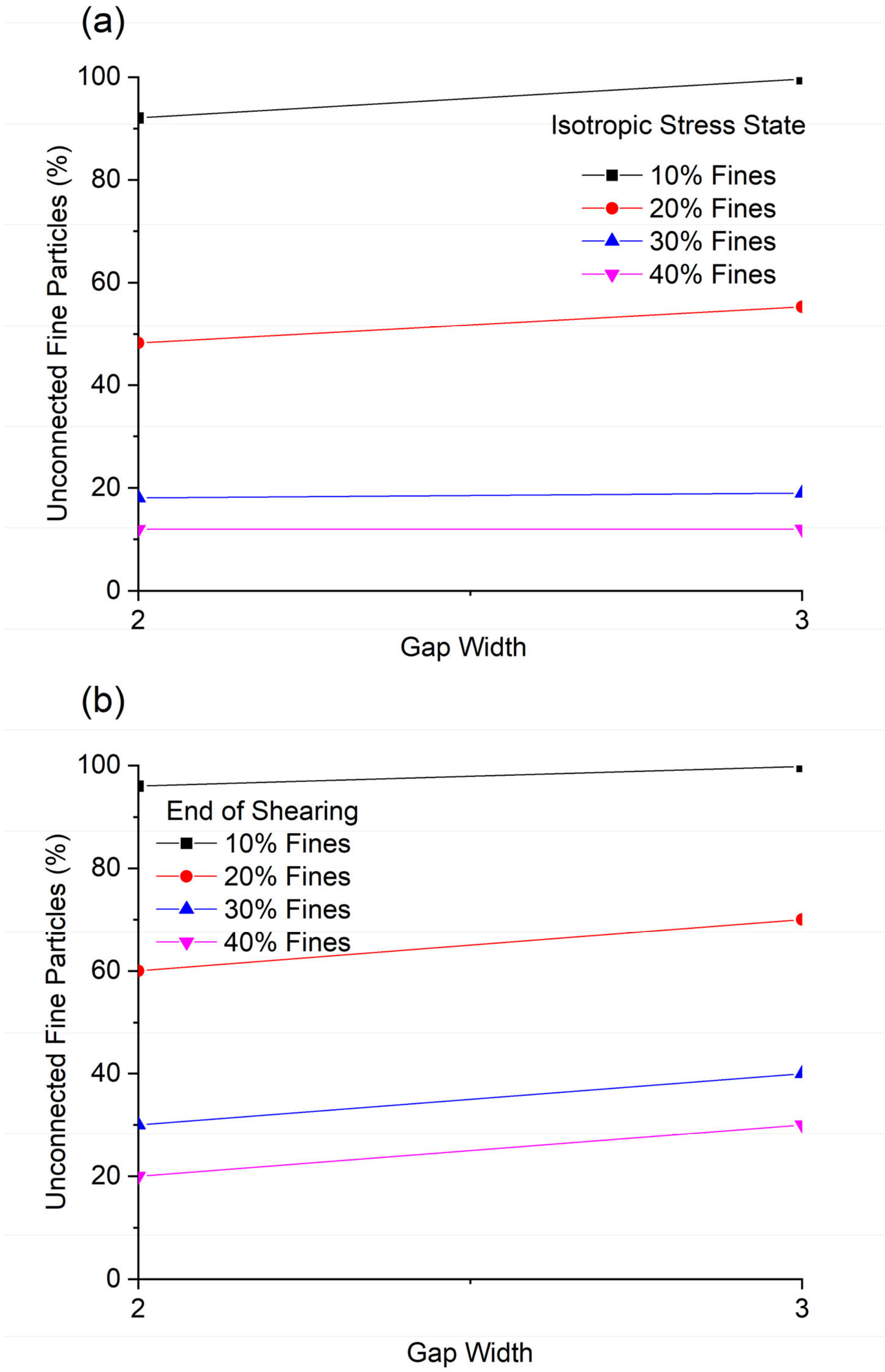

Fig. 8 The percentage (by number) of unconnected fine particles with different gap ratios and fines content (a) at the isotropic stress state, (b) at the end of shearing

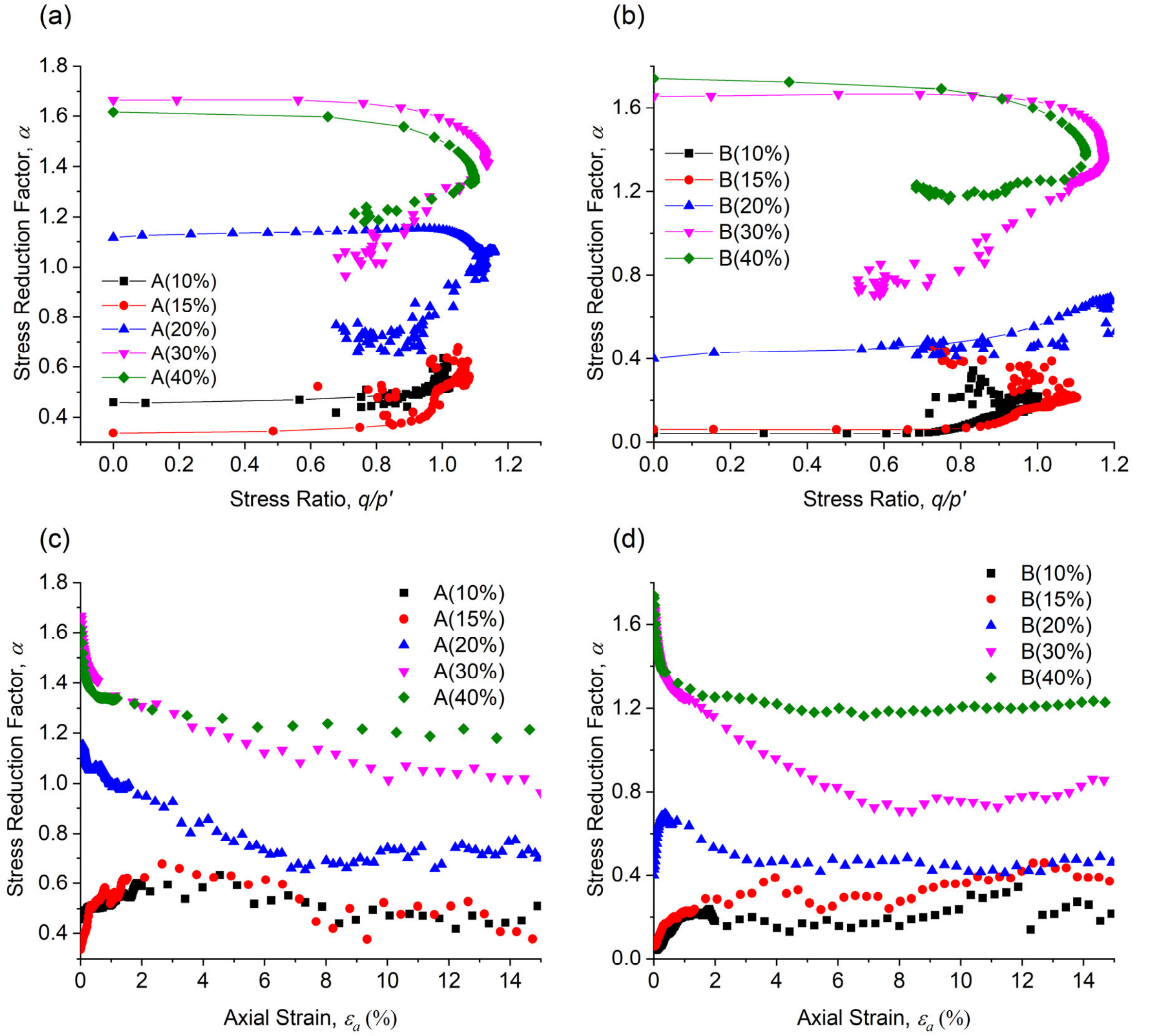

Fig. 9 (a), (b) Relationship between stress reduction factor (α) and stress ratio (q/p') for Specimens A and B, (c), (d) relationship between stress reduction factor (α) and axial strain (ε_a) for Specimens A and B.

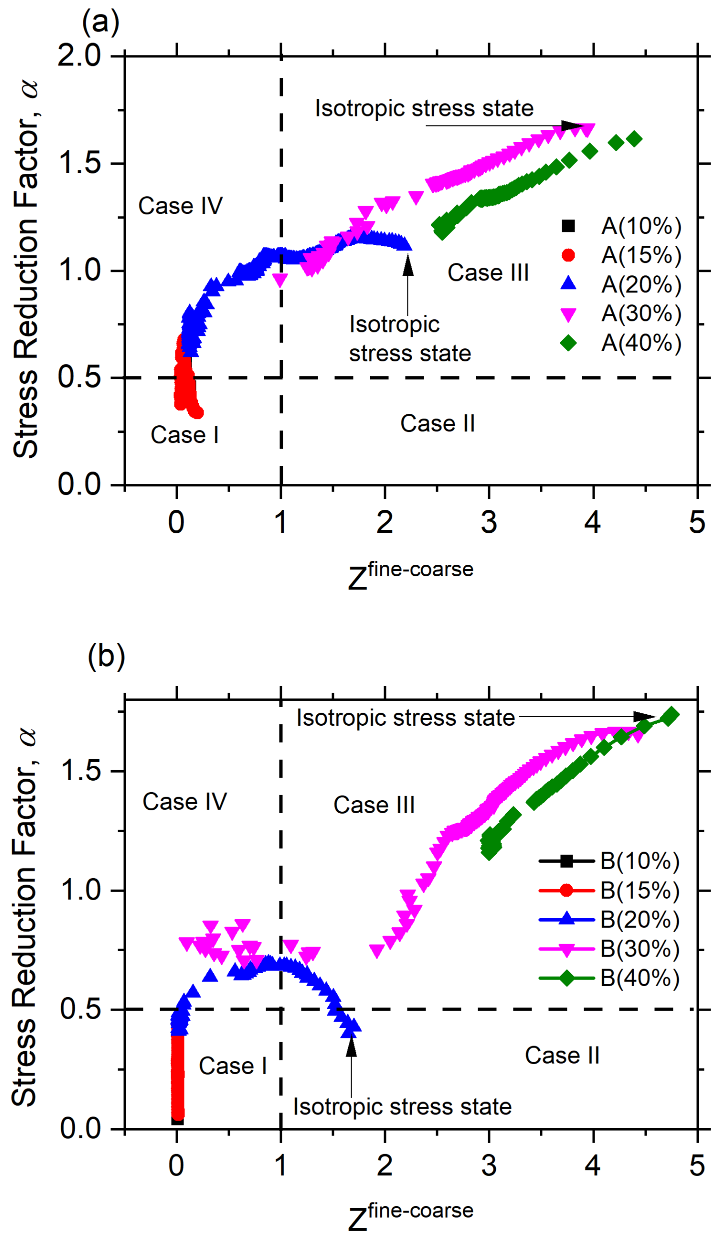

Fig. 10 Evolution of the stress reduction factor (α) with fine-coarse coordination number ($Z^{fine\text{-}coarse}$)

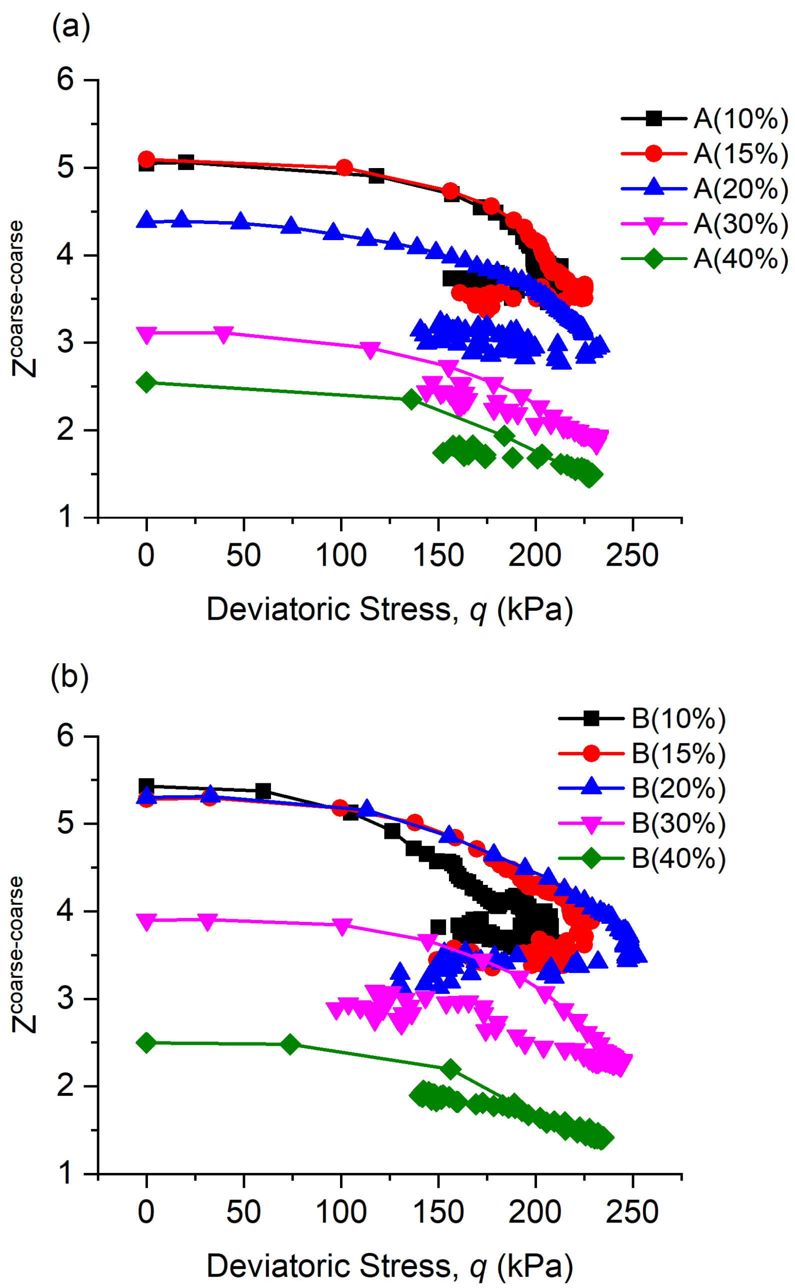

Fig. 11 Variation of the coarse-coarse coordination number ($Z_{coarse\text{-}coarse}$) with deviatoric stress

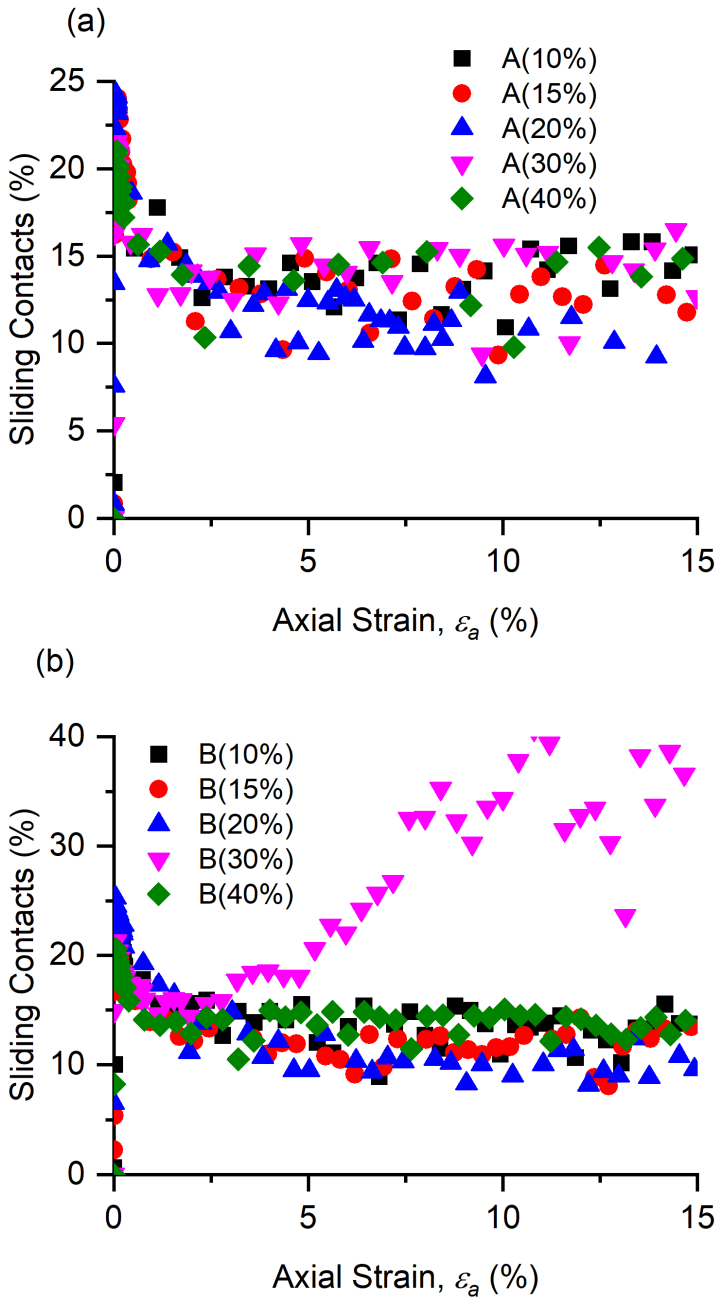

Fig. 12 Development of the proportion of sliding contacts with axial strain.

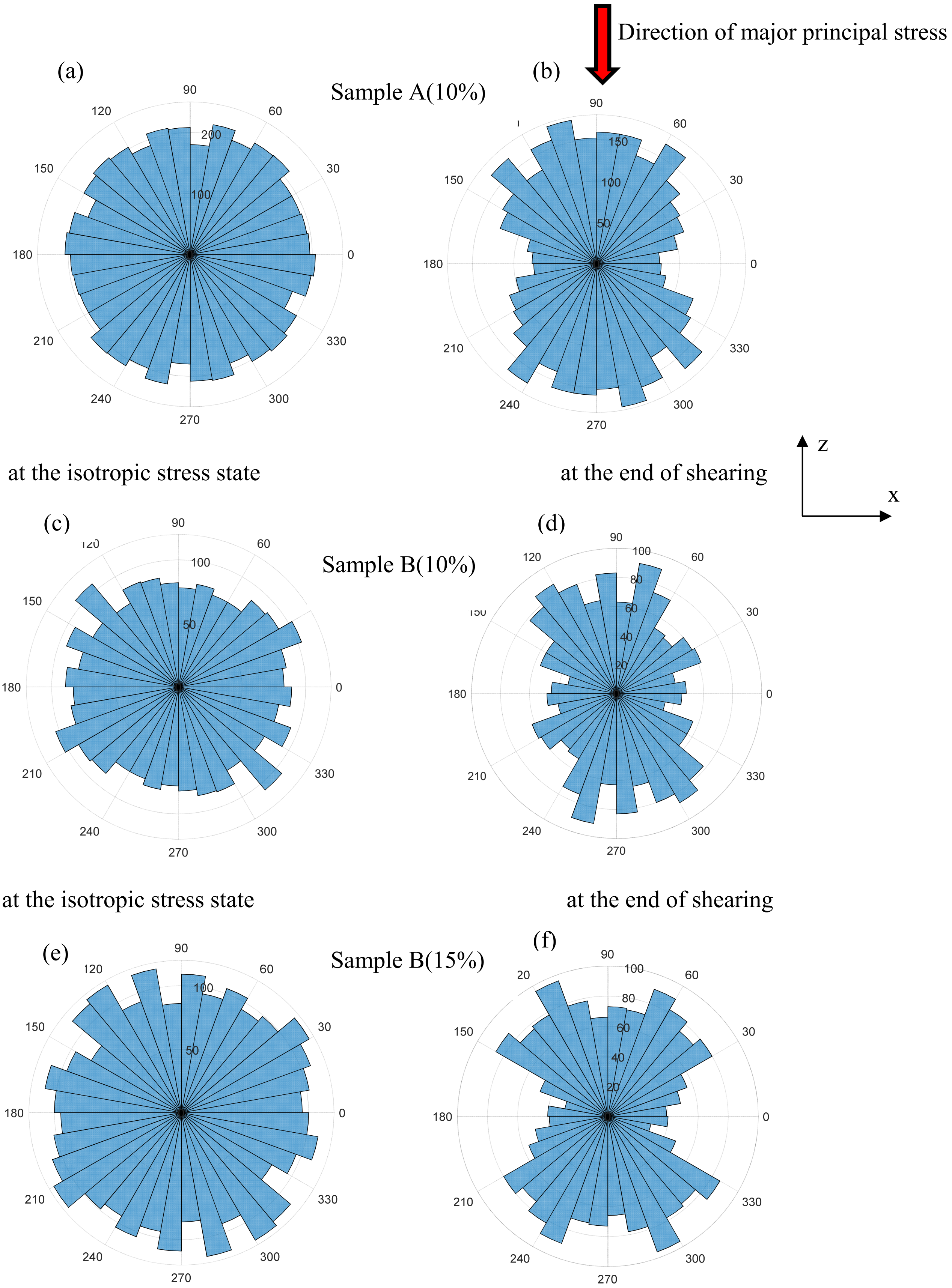

Fig. 13 Rose histograms of the contacts for selected Specimens 1(10%), 2(10%), and 2(15%)